Noname manuscript No.
(will be inserted by the editor)

Fault displacement modelling using 3D vector fields

Frode Georgsen · Per Røe · Anne Randi Syversveen · Oddvar Lia

Received: date / Accepted: date

Abstract In history matching and sensitivity analysis, flexibility in the structural modelling is of great importance. The ability to easily generate multiple realizations of the model will have impact both on the updating workflow in history matching and uncertainty studies based on Monte Carlo simulations.

The main contribution to fault modelling by the work presented in this paper is a new algorithm for calculating a 3D displacement field applicable to a wide range of faults due to a flexible representation. This gives the possibility to apply this field to change the displacement and thereby moving horizons and fault lines.

The fault is modelled by a parametric format where the fault has a reference plane defined by a centre point, dip and strike angles. The fault itself is represented as a surface defined by a function $z = f(x, y)$, where x, y and z are coordinates local to the reference plane, with the z-axis being normal to the plane.

The displacement associated with the fault outside the fault surface is described by a 3D vector field. The displacement on the fault surface can be found by identifying the intersection lines between horizons and the fault surface (fault lines), and using kriging techniques to fill in values at all points on the surface. Away from the fault surface the displacement field is defined by a monotonic decreasing function which ensures zero displacement at a specified distance from the fault.

An algorithm is developed where the displacement can be increased or decreased according to user-defined parameters. This means that the whole displacement field is changed and points on horizons around the fault can be moved accordingly by applying the modified displacement field on them. The interaction between several faults influencing the same points is taken care of by truncation rules and the ordering of the faults.

The method is demonstrated on a realistic synthetic case based on a real reservoir.

Keywords Fault modelling · Fault displacement · History matching · Uncertainty analysis

Frode Georgsen
Norwegian Computing Center
P.O.Box 114, Blindern
N-0314 Oslo, Norway Tel.: +47 22 85 25 00
Fax: +47 22 69 76 60
E-mail: frode.georgsen@nr.no

P. Røe
Norwegian Computing Center

A. R. Syversveen
Norwegian Computing Center

O. Lia
Statoil ASA

1 Introduction

Several authors have pointed out the need for building structural models that are well suited for performing uncertainty analysis on geological horizons and faults. Caumon et al. [4] use a set of techniques to model structural uncertainty by perturbing stochastically the geometry of a reference structural interpretation. This extends the work presented in Lecour et al. [11] where stochastic modelling of fault locations in reservoir grids is used to perform sensitivity studies on volume calculations in the 3D earth model. Thore et al. [19] underline the importance of assessing the sources of uncertainty in the structural modelling and show how this has impact on gross rock-volume calculations, well planning, flow

simulation and history matching. In Seiler et al. [17] and Seiler et al. [18] the structural uncertainty modelling is included in the history matching workflow by accounting for the uncertainty in horizon and fault modelling. Røe et al. [16] describe how the uncertainty associated with depth migration, seismic interpretation and well data can be incorporated in the structural modelling by presenting a flexible method for stochastic simulation of fault shape and position based on a parametric fault model. The same fault model is used in this work and is presented in Section 2 below.

Fault modelling is an important part of the structural modelling workflow. During the recent years, software and method development has made significant improvements in terms of better quality, faster model building and improved ability to update models. This is due to simplified workflows for modelling of fault surfaces and fault truncations. To perform a model update workflow through conditioning to dynamic data, like in Seiler et al. [18], or to perform static uncertainty studies, like in Caumon et al. [4], it is necessary to create multiple realizations of the model. In most cases this is not so easy. Interpretation and depth conversion uncertainties of fault surfaces and fault throw influence volume calculations of segmented reservoirs and flow across fault surfaces. It has been difficult to capture this uncertainty without much manual work to create alternative fault realizations. Very often this is not done, with the consequence that the effect of fault interpretation uncertainty is not known or ignored.

In the present paper, several elements relevant for dynamic flow properties and volumetric estimation with uncertainty are addressed. These include the position of faults and horizons, the magnitude of the displacement caused by the faulting process and the impact this has on the sealing effects and facies distribution around the faults. By using a parametric fault model, it is possible to modify an existing realization of fault surfaces and fault throw simply by modifying some model parameters instead of editing model input data manually or by scripts. This makes it possible to include fault modelling into Monte Carlo simulations or history matching loops in order to estimate the effect of fault interpretation uncertainty and throw on reservoir volumes and flow. Seiler et al. [18] show how changing the fault throw and fault position can be used to update the structural model in a history matching workflow. This is performed with the pillar-based fault model Havana, presented in Hollund et al. [10], by scaling the displacement operator and moving the fault pillars. The same fault model is used in Rivenæs et al. [14] to show how the uncertainty in fault properties for both faults on the limit of seismic resolution and faults with throw below seismic resolution affect the flow properties in different well drilling scenarios. With a new and more flexible surface based fault model, these operations will become easier to perform.

An algorithm for creating a 3D displacement field associated with a single fault plane is presented. The chosen fault representation permits perturbing the dip, strike and location of the fault, while the 3D displacement field is used to move horizons representing the effect of a change in fault throw. Mallet [12] defines a similar transformation into an unfaulted space, while the present paper focus on having a displacement operator for each individual fault. The joint effect from faults close to each other is taken care of by truncation rules applied on the fault operator defined from the displacement fields. Caumon et al. [4], Lecour et al. [11] and Holden et al. [9] focus on stochastic perturbation of fault geometries and fault throw, but in a history matching workflow a deterministic way of perturbing the fault geometry and throw is desired. Effects of changing fault throw on reservoir flow can implicitly be represented by changing the throw used in the fault seal calculations as shown by Manzocchi et al. [13], however, an explicit change of fault throw is needed for volume calculations and for well planning.

2 Surface based fault model

Several approaches to model faults are in use, with each type of model having certain advantages and certain disadvantages. In Hollund et al. [10] and Holden et al. [9], faults are modelled by bilinear planes connected with pillars. This represents an easy format to operate on if geological structures are not too complicated and it ensures correspondence between fault representation and the reservoir grid. However, this format is not very flexible and does not capture more complex structures like, for instance, listric faults. The concept of modelling faults as triangulated surfaces is presented in Caumon et al. [3] and Caumon et al. [5]. This format allows for modelling with geological realism and capture complicated geological features. The cost to this might be loss in flexibility and speed compared to a parametric approach.

In the model presented in this paper, the fault is represented by a fault surface along the same lines as in Hoffman and Neave [8]. Each fault is related to a reference plane defined by a strike angle (θ) and dip angle (ϕ) as illustrated in Figure 1. On this plane a reference point (X_0, Y_0, Z_0), given in global coordinates, is defined. The strike, dip and reference point define a local coordinate system used for all operations on the

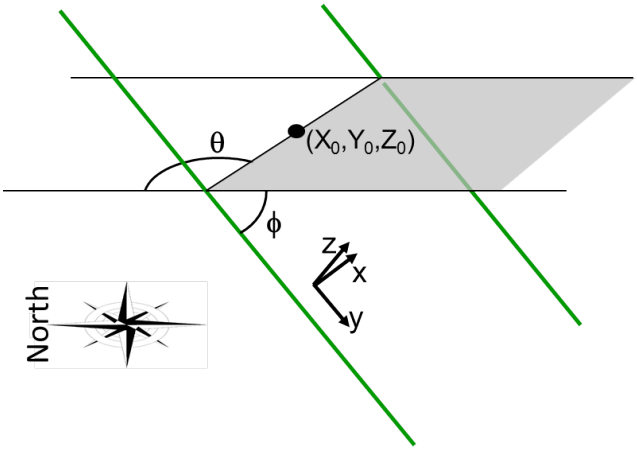

Fig. 1 Local coordinate system (x, y, z) defined by reference point (X_0, Y_0, Z_0), fault strike angle θ and dip angle ϕ. The z-axis points in hanging wall direction. The edges of the reference plane is drawn by green lines.

fault. The transformation from global (X, Y, Z) to local coordinates (x, y, z) is given by

$$\begin{bmatrix} x \\ y \\ z \end{bmatrix} = \begin{bmatrix} \sin\theta & \cos\theta & 0 \\ \cos\theta\cos\phi & -\sin\theta\cos\phi & \sin\phi \\ \cos\theta\sin\phi & \sin\theta\sin\phi & -\cos\phi \end{bmatrix} \begin{bmatrix} X - X_0 \\ Y - Y_0 \\ Z - Z_0 \end{bmatrix} \tag{1}$$

with the positive z-axis pointing in the hanging wall direction.

The fault surface is defined as a function $z = f(x, y)$ for all (x, y) on the reference plane. The value of f is the deviation from the reference plane along the z-axis (i.e. normal to the reference plane). This means that for each (x, y) only one value of $f(x, y)$ is defined, giving only one position for the fault surface. Figure 2 shows the vertical cross section at $x = x'$ where the fault surface is represented by $f(x', y)$ as the deviation from the reference plane. In the computer representation of the fault model, $f(x, y)$ is represented as a set of z-values corresponding to the nodes of a regular 2D grid in the reference plane.

This surface based fault model is well suited for several of the operations on faults that will typically be part of uncertainty studies. Moving the fault or rotating it in strike or dip direction is easily accomplished by changing parameter values, and several realizations can be generated by varying one or more parameters according to user-specified random distributions.

Like in the Havana model presented in Holden et al. [9] and Hollund et al. [10] the surface based fault model is not only represented by the fault surface, but also by a 3D fault operator affecting the volume around the fault. This operator is represented by a 3D displacement vector field presented in the next section.

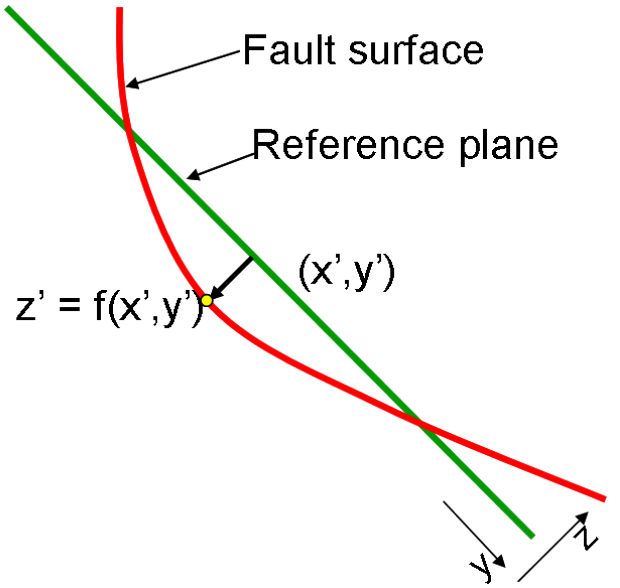

Fig. 2 Vertical cross section through the fault at $x = x'$. The fault surface (in red) is represented by the function $z = f(x', y)$ as the deviation from the reference plane (in green) along the z-axis.

3 3D displacement vector field

The fault incidence is a complicated event carried out through several steps where every mathematical formulation is a simplification. The displacement of rock caused by the faulting can be looked upon as a continuous process in the sense that two neighbouring points before the fault incidence, are also neighbours afterwards due to the nature of the hard material involved. This suggests that the faulting operation can be described by a vector field defined on the whole volume affected by the fault. Every single point in the volume is moved along a 3D vector from its original position to the faulted position, and the whole vector field can be constructed by the assumption of continuity. For simplification in the following, only dip-slip faults are considered. This means that the displacement on the fault surface can be modelled by one 2D displacement field and the displacement away from the fault surface as a function of this. If slip also in strike direction should be accounted for, an additional 2D displacement field would have been necessary. The next section describes how the 2D displacement field can be constructed from intersection points between horizons and faults.

3.1 Constructing 2D displacement fields from fault lines

By identifying fault lines, defined as intersection lines between horizons and the fault surface, information

about fault displacement along the fault surface can be found. Figure 3 shows an example of fault lines from a structural model where the interpreted horizon intersects the fault surface. The fault line is shown in green with straight line on the foot wall side and dashed line on the hanging wall side. The displacement is measured

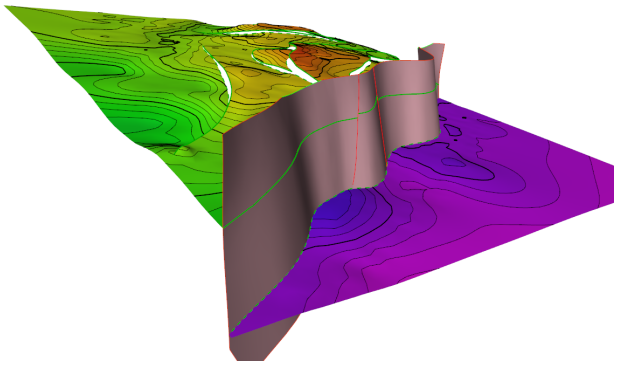

Fig. 3 Fault lines shown in green on the fault surface. Straight line on the foot wall side and dashed line on the hanging wall side.

along the reference plane. For a linear fault this reference plane coincides with the fault surface as illustrated in Figure 4. For the general non-linear case the displace-

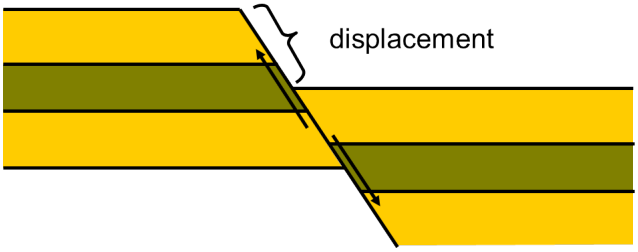

Fig. 4 Displacement illustrated on a linear fault. The displacement is measured along the reference plane which in this case coincide with the fault surface.

ment is measured as the distance between the point where the horizon intersects the fault on the foot wall side projected down to the y-axis and the point where the horizon intersects the fault on the hanging wall side projected down to the y-axis. This is illustrated in Figure 5 for two horizons H_1 and H_2 in a vertical cross section at $x = x'$. This gives displacement values d_1 and d_2 for the horizons H_1 and H_2 respectively. The displacement value is found as the y-value for the foot wall intersection point subtracted the y-value for the hanging wall intersection point giving positive values for normal faults and negative values for reverse faults. With this definition, the fault throw is the vertical projection of the displacement.

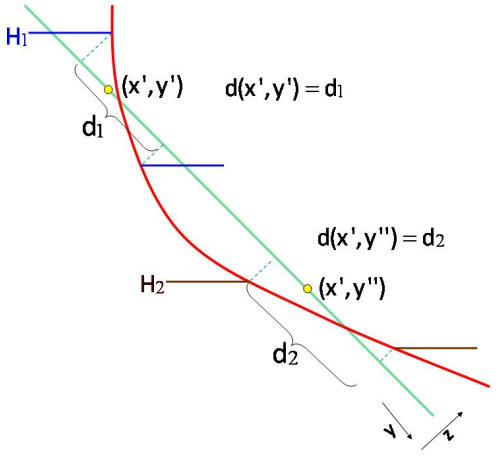

Fig. 5 Vertical cross section showing how the values for the 2D displacement field $d(x, y)$ defined on the fault surface is calculated from fault line information.

The 2D displacement field on the fault reference plane is denoted $d(x, y)$ and a regular 2D-grid is defined in the xy-plane. For each fault a hanging wall(HW) / foot wall(FW) displacement ratio can be found, either based on theoretical considerations or estimated from data. According to Gibson et al. [6], this ratio can be predicted from the fault dip. This displacement ratio, given as a user-specified parameter $\gamma \in [0, 1]$, is used to populate the 2D displacement grid. $\gamma = 1$ and $\gamma = 0$ means that all displacement is on the hanging wall side and foot wall side respectively. The displacement observed from fault lines and the value for the HW/FW displacement ratio gives an estimate for the position where the original (unfaulted) horizon intersects the fault surface with the associated displacement value.

The HW/FW displacement ratio for the fault in Figure 5 is 0.7, meaning that most of the displacement is on the hanging wall side. This defines the positions $f(x', y')$ and $f(x', y'')$ where the unfaulted version of horizons H_1 and H_2 cross the fault surface. The values for the displacement function d are identified as $d(x', y') = d_1$ and $d(x', y'') = d_2$.

The displacement values associated from fault lines constitute a set $\mathbf{d} = \{d(x_1, y_1), d(x_2, y_2), \ldots, d(x_n, y_n)\}$ of known values for the 2D displacement field. These are used in simple kriging to populate the whole field. Simple kriging is a linear interpolation technique used to estimate the value of an unknown function at a location given known values, a trend and a spatial covariance structure. See Goovaerts [7] for a detailed description on kriging. The estimation of the trend is described in

Section 3.2. The kriging equation for the unknown value $d^*(x, y)$ of the displacement field at location (x, y) is

$$d^*(x, y) = \mu(x, y) + \mathbf{k}\mathbf{K}^{-1}(\mathbf{d} - \boldsymbol{\mu}), \quad (2)$$

where $\mu(x, y)$ is the trend value, $\mathbf{k} = \{\mathrm{Cov}(x_1 - x, y_1 - y), \ldots, \mathrm{Cov}(x_n - x, y_n - y)\}$ is the vector of covariances between the location (x, y) and the locations of the known displacement values, $\mathbf{K}$ is the covariance matrix for the known displacement values, $\mathbf{d}$, and $\boldsymbol{\mu}$ is the vector of the trend values at the locations of the known displacement values. The covariance structure is defined by a variogram function with user-specified standard deviation, shape and ranges. The correlation structure is assumed stationary, but the standard deviation may vary, with lower values in areas with lot of data, and decreasing to zero towards the fault tip-line.

3.2 Trend estimation

The trend function for the displacement is given by an ellipse with centre point (x_0, y_0), length (l_x) in strike direction and height (l_y) in dip direction. Argumentation for the elliptic shape of the fault displacement is found in Barnett et al. [1] and Walsh and Watterson [22]. The ideal, theoretical case has maximum displacement at the centre point and zero displacement reached at the elliptic tip-line. The normalized displacement profile used in the present model is found in Walsh and Watterson [21] and is given by

$$\mu_0(x, y) = 2 \cdot (1 - r(x, y)) \cdot \sqrt{\frac{(1 + r(x, y))^2}{4} - r(x, y)^2}, \quad (3)$$

where $r(x, y) = \sqrt{\left(\frac{x - x_0}{l_x}\right)^2 + \left(\frac{y - y_0}{l_y}\right)^2}$ is the normalized radial distance from the centre. The tip-line is the elliptic line defined by $r(x, y) = 1$. Outside this line the trend equals zero. Let d_{max} be the maximum displacement assumed at the centre of the ellipse. This gives the trend function $\mu(x, y) = d_{max}\mu_0(x, y)$. Prior information on the relationship between the maximum displacement and the length of the ellipse and the relationship between the length and the height is provided as user input. A discussion on these parameters can be found in Walsh and Watterson [22].

The algorithm used for estimating the parameters in the trend function is as follows:

1. Find the maximum of the known displacement values and use this as an initial guess for d_{max}.
2. Find initial guesses for l_x and l_y based on the prior information for the relationships between d_{max}, l_x and l_y.
3. Find the optimal position of the ellipse centre by minimizing the sum of squared errors between the displacement and the trend over all points $(x_1, y_1), \ldots (x_n, y_n)$ with respect to (x_0, y_0).
4. Use the optimal ellipse centre and find the optimal length and height by minimizing the sum of squared errors with respect to l_x and l_y.
5. Use the linear regression model

$$d(x_i, y_i) = d_{max}\mu_0(x_i, y_i) + \epsilon(x_i, y_i)\ i = 1, \ldots n \quad (4)$$

with residuals $\epsilon(x_i, y_i)$ to find least squares estimate for d_{max} as $(\sum x_i^2)(\sum x_i y_i)^{-1}$.

For illustration, the Emerald field reservoir model, which is one of the tutorial examples of the reservoir modelling software RMS (Roxar [15]), has been chosen. Figure 6 shows the structural model for the Emerald field indicating one large truncating fault (F1), and one smaller fault (F2) which is truncated by F1. There are four horizons in the model, and the fault lines for these horizons are drawn on the fault surfaces. The upper four lines represent the intersection between the horizons and the fault on the foot wall side and the lower four lines represent the intersection between the horizons and the fault on the hanging wall side. The differences between lines of identical colours represent the displacements and the large displacement on F1 is clearly visible.

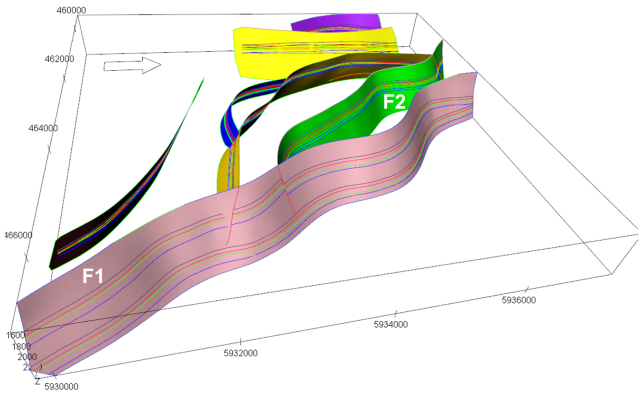

Fig. 6 The Emerald field structural model with fault lines for four horizons drawn on each fault surface.

Figure 7 shows the F1 fault with displacement values found from fault lines as described above. The HW/FW displacement ratio is 0.7. The dots represent grid nodes in the local 2D grid, with coloured nodes representing known displacement values. The maximum displacement value, located in the pink area, is 590 meters.

A trend field for the displacement is estimated using the algorithm described above. The trend is shown

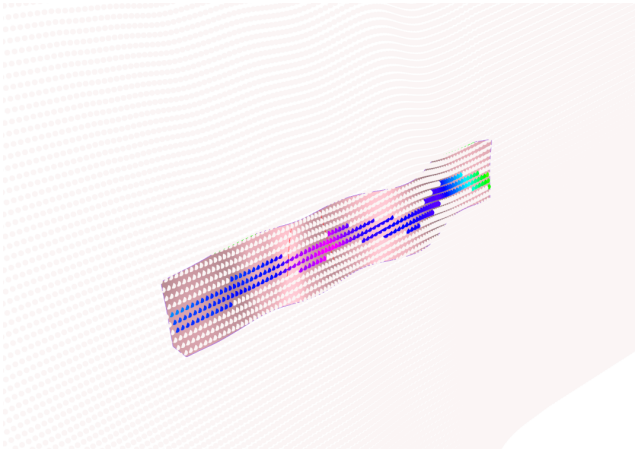

Fig. 7 The fault F1 from the Emerald field structural model with dots representing nodes in local regular 2D grid. The coloured nodes represent known displacement values found from fault lines.

in Figure 8. The elliptical shape of the trend is clearly visible. It is also obvious that the estimated length and height of this ellipse by far extend the actually modelled fault. This reflects the large displacement in the limited area where there are actually identified fault lines. A priori the length of the ellipse is assumed to be 20 times the maximum displacement, and the height is assumed to be half the length. The centre of the trend ellipse is estimated to be further north-east than the location of the maximum value found from fault lines. The maximum displacement in the trend ellipse is estimated to 545 meters.

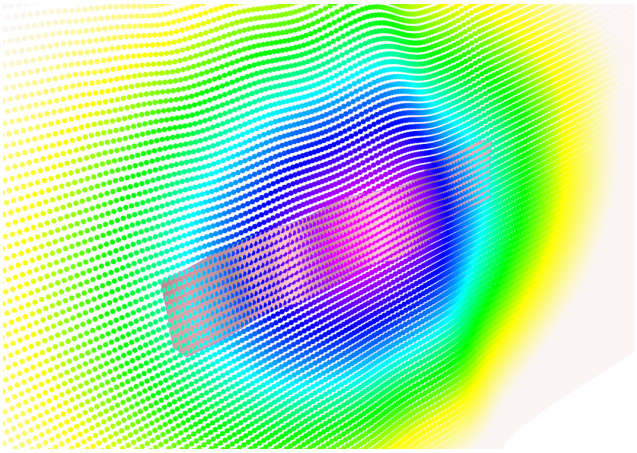

Fig. 8 The fault F1 from the Emerald field structural model with the elliptical trend estimated from the data and apriori parameters.

The result of the kriging with the elliptical trend and the known displacement values is shown in Figure 9. The correlation structure follows a spherical variogram with a range of 2000 meter in strike direction (x) and 1000 meter in dip direction (y). This displacement field corresponds exactly to the known values at the locations where these are found. Since the ellipse centre for the trend does not coincide with the maximum known value, the high displacement values are shifted to south-west along the fault.

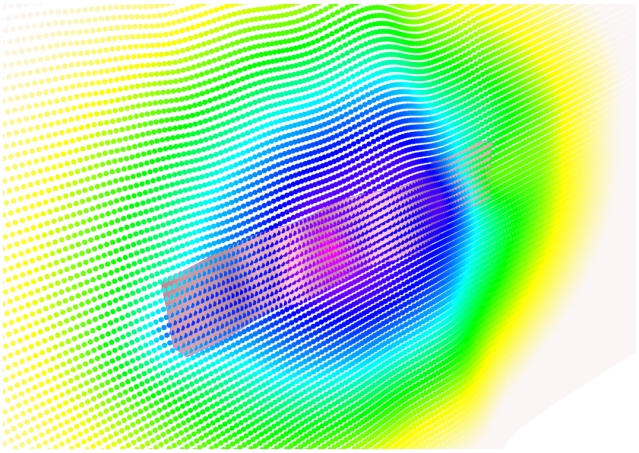

Fig. 9 The fault F1 from the Emerald field structural model with the displacement field calculated by kriging.

3.3 Displacement field in volume around the fault surface

The displacement decreases away from the fault surface until it dies out at the reverse drag radius (Barnett et al. [1]). This decrease is non-linear, and along the z-direction the profile follows the curve suggested in Cardozo et al. [2], and given by

$$\alpha(x,y,z) = \left(1 - \frac{|z - f(x,y)|}{R}\right)^2, \tag{5}$$

where R is the reverse drag radius. This profile is illustrated in Figure 10. The full 3D displacement field is defined as a vector field, with a vector

$$\begin{aligned}&\mathbf{D}(x,y,z)\\ &= \{D_x(x,y,z)\mathbf{u}_x, D_y(x,y,z)\mathbf{u}_y, D_z(x,y,z)\mathbf{u}_z\}\end{aligned} \tag{6}$$

for each spatial location. Here $\mathbf{u}_x, \mathbf{u}_y, \mathbf{u}_z$ are unit vectors along the x-, y- and z-axes respectively. The x-component D_x is in the present model defined to be zero everywhere, reflecting that there is no strike-slip displacement. This is done for implementation simplicity and is not a necessary limitation for the model. The y-component, D_y has different expression on the hanging wall and foot wall sides. For $0 < z - f(x,y) < R$,

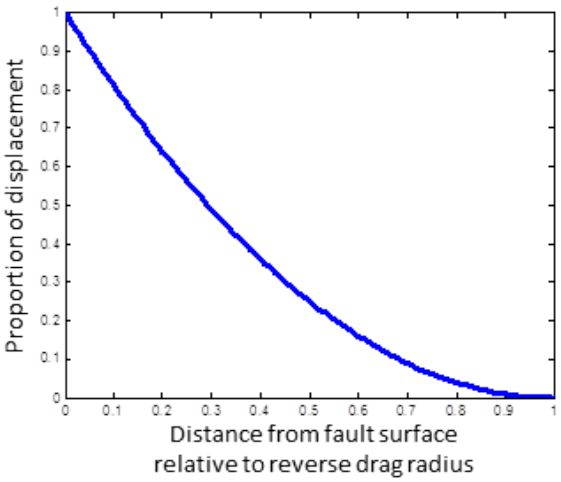

Fig. 10 The profile for the displacement decrease in the normal direction away from the fault surface. The horizontal axis shows the distance from the fault surface with 1.0 being at the reverse drag radius. The vertical axis shows the proportion of the fault surface displacement at the normal projection of the point.

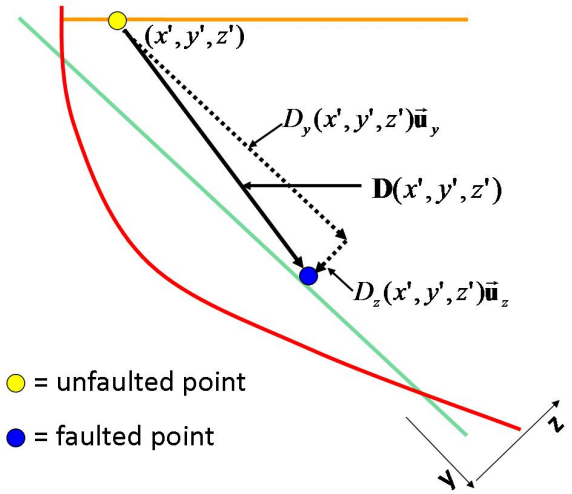

Fig. 11 Vertical cross section showing the 3D displacement vector **D** decomposed into D_y and D_z and the position of a point before and after the fault incidence.

that is within the reverse drag radius on the hanging wall side, the expression is

$$D_y(x, y, z) = \gamma \cdot d(x, y) \cdot \alpha(x, y, z) \tag{7}$$

giving positive values for normal faults and negative values for reverse faults. For $-R < z - f(x, y) < 0$, that is within the reverse drag radius on the foot wall side, the expression is

$$D_y(x, y) = (\gamma - 1) \cdot d(x, y) \cdot \alpha(x, y, z) \tag{8}$$

giving negative values for normal faults and positive values for reverse faults. The z-component is given by

$$D_z(x, y, z) = f(x, y + D_y(x, y, z)) - f(x, y), \tag{9}$$

implying that the distance from the point to the fault surface (along the normal) remains constant through the displacement operation.

Figure 11 shows a vertical cross section at $x = x'$ with the D_y- and D_z-components of the displacement vector **D**. The position of an arbitrary point away from the fault surface before and after the fault incident is shown.

The effect of the 3D displacement operator is shown in Figures 12 and 13 for a linear and a listric fault respectively and with different parameter values. Figure 12 shows an example with six horizons and a planar fault where the displacement is equally distributed on hanging wall and foot wall sides ($\gamma = 0.5$) and where the reverse drag radius is 1000 m in one case and 3000 m in the other.

In Figure 13 six horizons are subject to a listric fault with all displacement on the hanging wall side and with two different reverse drag radii.

4 Truncations and interactions between faults

Truncations in the present fault model are specified in pairs of truncating and truncated faults giving a set of truncation rules. For each pair an indicator specifies if the fault is truncated on the hanging wall or foot wall side of the truncating fault. Two faults intersecting each other do not necessarily define a truncation, so the model has flexibility to handle both λ-, y- and x-faults. This means that the truncation rules are applied to join fault blocks together in a specific fault network representation. This is partly what is described as the fused fault block approach in Hoffman and Neave [8]. The displacement field for the truncated fault is also truncated. This is illustrated in Figure 14 showing two faults where the smaller is truncated by the larger. All displacement is on the hanging wall side for both faults. The volume affected by the displacement operator of the larger fault is shown in green in the upper picture, while the volume affected by the displacement operator of the smaller truncated fault is shown in red in the lower picture.

Figure 15 shows the effect of truncation on the estimated displacement field for fault F2 in the Emerald model. This fault is truncated by F1. The upper figure shows the displacement field for F2 without taking the truncation into account, while the lower figure shows the displacement field when accounting for the truncation by F1.

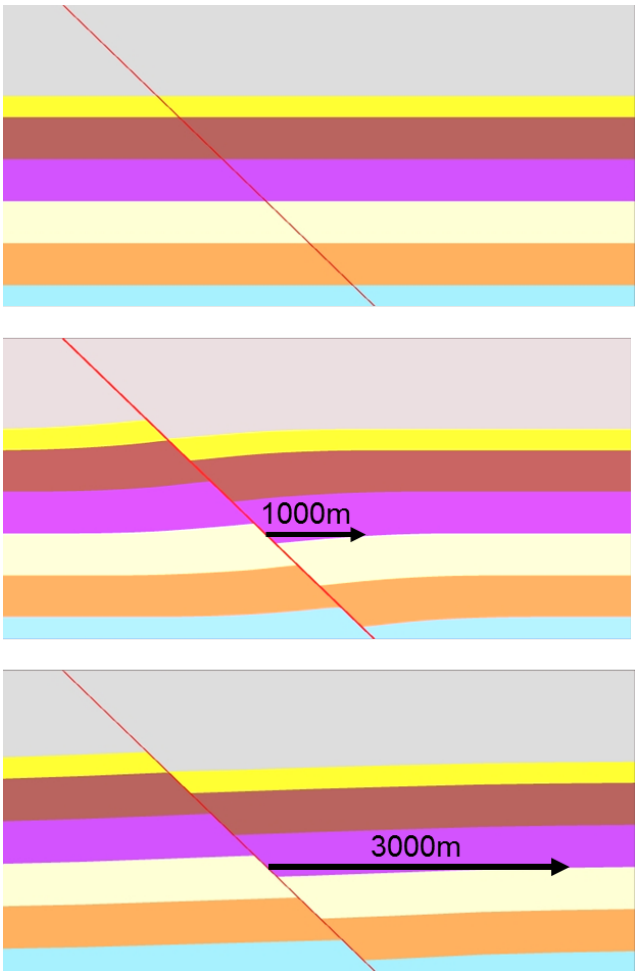

Fig. 12 : Effect of displacement operator on a linear fault with displacement equally distributed to hanging wall and foot wall sides. Upper: Unfaulted. Middle: Faulted with reverse drag radius 1000m. Lower: Faulted with reverse drag radius 3000m.

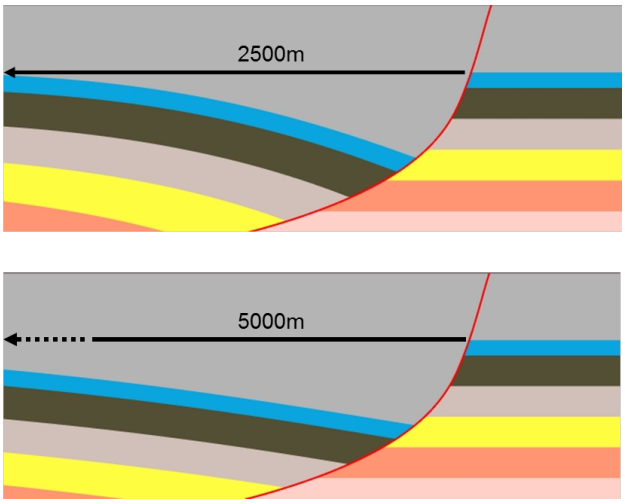

Fig. 13 Effect of displacement operator on a listric fault with all displacement on hanging wall side. Upper: Reverse drag radius 2500 m. Lower: Reverse drag radius 5000m.

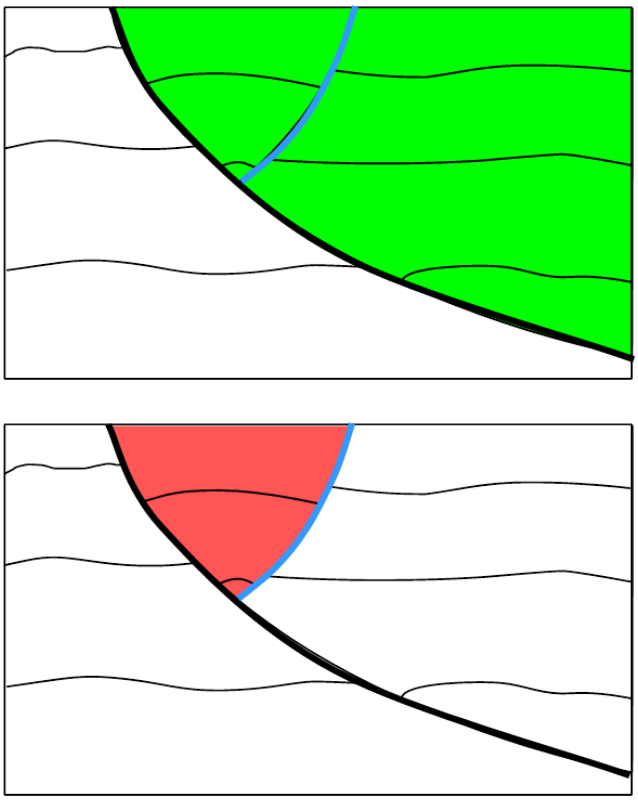

Fig. 14 Volume affected by the displacement of the large, truncating fault in green and volume affected by the displacement of the smaller, truncated fault in red.

The truncation rules can be applied to define an ordering of faults. This is based on the principle that a truncating fault is older than the faults it truncates. The fault lines from the structural model represent the net effect of the displacement from several faults. To find the fault lines representing the actual displacement from the fault when the fault incident occured, a sequential restoration of the faults is needed. The fault lines from the youngest fault is in this sense correct and the displacement field for this fault can be generated without modifications. If the fault lines from the second youngest fault are influence by the younger, these must be restored back to its original position by applying a reverse fault operator for the youngest fault. These restored fault lines are then used for generating the displacement field for this second fault. This procedure is applied to all faults in the correct order. Figure 16 shows the original foot wall fault lines (in green) for two horizons of the fault F1 in the Emerald model together with the restored fault lines (in black). At the intersection with the two truncated faults (F2 and F3) the effects of the truncations is removed giving continuity in the restored fault lines. At the truncation with F3, the restored fault line is lifted up to the level at the

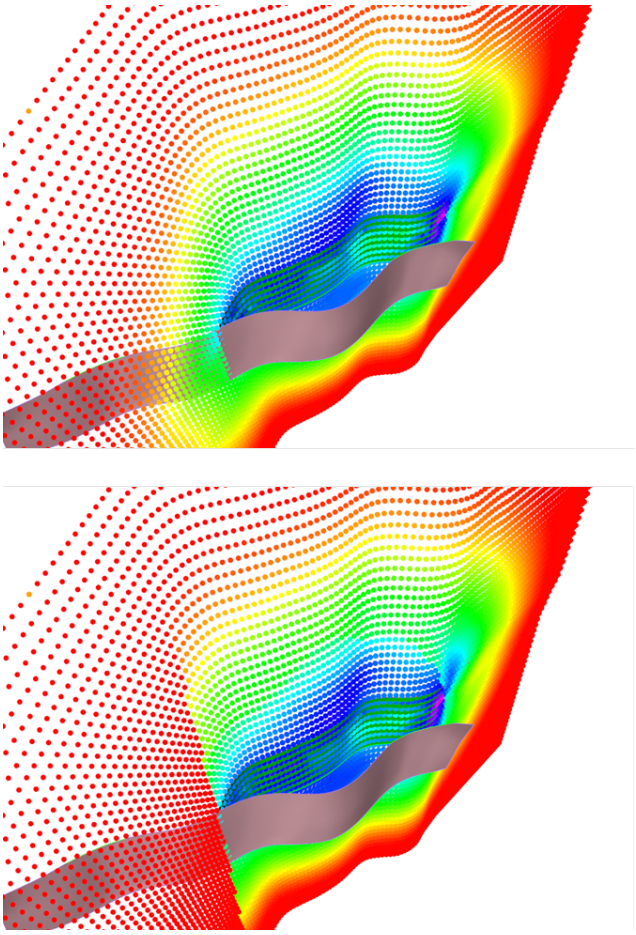

Fig. 15 Emerald model showing displacement field for fault F2. In the upper figure the truncation by fault F1 is not accounted for in the displacement field. To the right the displacement field is truncated by F1.

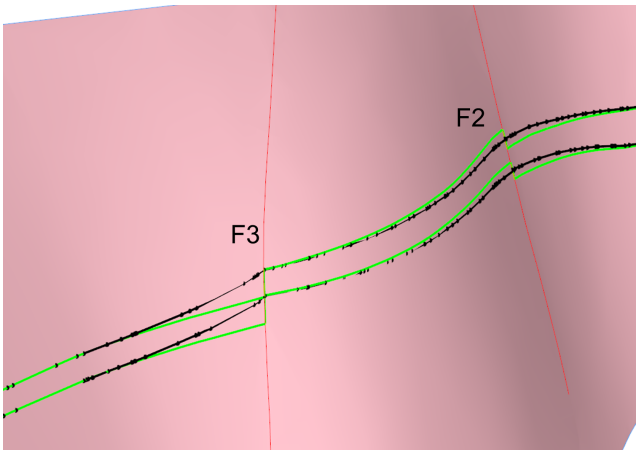

Fig. 16 Fault lines for the foot wall side of the fault F1 in the Emerald model. Green lines show the original fault lines from the structural modelling with discontinuity at the intersections with the truncated faults F2 and F3. The black lines show the fault lines after the effect of the truncations is removed. Away from the truncations the original and restored fault lines coincide.

foot wall side of F3. This is because the hanging wall / foot wall displacement ratio for F3 is 1.0, meaning that all the displacement is on hanging wall side. At the intersection with F2 the restored fault lines lie between the original ones meaning that the displacement for F2 is equally distributed on both sides.

Since every point in the reservoir volume might be affected by the displacement from several faults, a net displacement vector for the point should account for the joint effect from the displacement of all faults that influence the point. The net displacement operator is found by applying the displacement operator for each individual fault to the point sequentially from the oldest to the youngest fault.

In the restoration, or de-faulting operation, a reverse fault operator is needed. To find an explicit expression for the inverse of the 3D displacement vector $\mathbf{D}$ defined by expressions (6) - (9) is not possible since there is no closed expression giving $d(x, y)$ as a function of y. This gives an undefined equation set. One possible solution is to create a 3D grid for the volume influenced by the fault and calculate the faulted position for each node in the grid. The inverse operator is then defined by mapping back from the cube of faulted positions using interpolation. With many faults, however, this is both memory- and CPU-demanding. The alternative approach, which is actually used, is to calculate the inverse of the 2D displacement function $d(x, y)$ as one grid for hanging wall side and one grid for foot wall side. The faulted point is projected onto the fault surface and the inverse 2D function is used by taking into account the side of the fault and the distance to the fault surface. Since this will only give correct answer for constant displacement, an iterative approach using binary search is used until the deviation from the correct point is within some predefined tolerance level. The displacement function is assumed to be quite smooth, so this approach gives a reasonably precise and fast approximation.

5 Applications of 3D displacement field

The horizon interpretations near faults has normally larger uncertainty than away from faults. The horizons are often based on extrapolation from interpreted seismic surfaces. Using the fault lines based on these interpretations to generate a displacement field gives a tool for quality control by analyzing the displacements. Improving the horizon modelling close to faults can have important impact on the modelling of fluid flow across faults (Hollund et al. [10]), well planning (Rivenæs et al. [14]) and fault sealing properties (Yielding et al. [20]), to mention just a few applications.

One of the advantages of having a fault model with a 3D displacement field explicitly defined, is the possibility of easily modifying the fault by changing the displacement. By the model presented above, the whole 3D displacement field can easily be changed by either scaling it with a factor, or by adding a constant to the 2D displacement field. This can be applied in a deterministic setting where the displacement is set to vary for example between minimum, maximum and best guess values, or in a stochastic setting where several realizations are generated by Monte Carlo simulations. Every modification of the displacement field means that all points in the influence area of the fault are moved. Section 6 shows examples of the effect of changing displacements by moving the points on the horizons in accordance with the modified fault operator after changing the displacement fields. The main steps in the algorithm for moving a point is to first reverse the faulting operation by moving the point back to its original (pre-faulted) position. The point is then moved to its modified (faulted) position by applying the modified displacement vector using expressions (6) - (9).

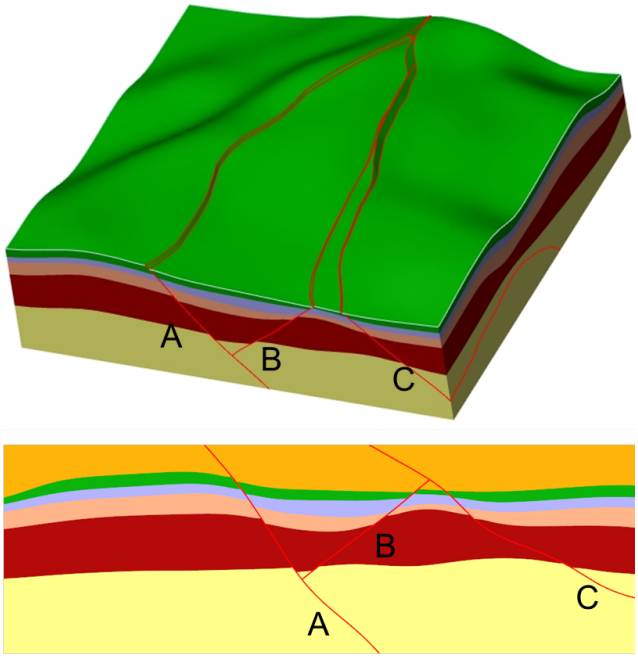

Fig. 17 Original position of horizons and faults. Faults A and B form a Y. Faults B and C form a λ. Fault C truncates faults A and B, while fault A truncates fault B. Upper: 3D cube with horizons and faults. Lower: Vertical cross section.

6 Examples from a synthetic case based on real reservoir

The effect of the 3D displacement operator described above is demonstrated on a synthetic reservoir with elements from a real case. There are three faults in the reservoir box, named A (to the left in the figures), B (middle) and C (right). The faults A and B form a Y, while B and C form a λ. C truncates both A and B, while A truncates B. The original state of the reservoir structure is shown in Figure 17. The figure shows the three faults in a 3D cube with the reservoir layers and in a vertical cross section.

The fault pattern defines four fault blocks shown in Figure 18.

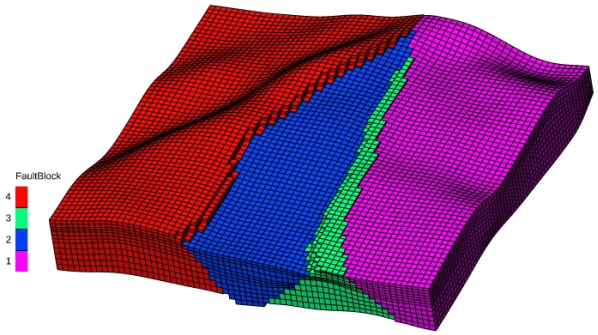

Fig. 18 Example reservoir consisting of three faults dividing the volume in four fault blocks.

Figure 19 shows the effect of changing the displacement for Fault A by a factor of 3 with all displacement on the hanging wall side. In the upper figure the effect is shown in a 3D cube of the whole reservoir box,while the lower figure shows a vertical cross section.

In Figure 20 both Fault A and Fault B have changed displacement by a factor of 3. For fault A the displacement is equally distributed on hanging wall and foot wall side, while for Fault B all displacement is on hanging wall side. The two faults have equal reverse drag radius. The figure shows the joint effect this has on the position of the horizons. The displacement change applied to Fault B affects only the fault block between Fault A and Fault B since Fault B is truncated by Fault A, while the change applied to Fault A also has an effect to the right of Fault B since there is no truncation at Fault B. The algorithm works such that the moving of points due to the change of displacement is first applied to the youngest fault (in this case Fault B) and then to the older (Fault A).

Figure 21 shows the gridded reservoir with colours of grid cells indicating the distance the cells has been moved as an effect of changing the displacements. The warmer colours mean downward displacement, while cold means upward. The upper figure shows the case where only Fault A has changed displacement. Cells on both sides of the fault are influenced. The lower figure shows the case where both fault A and fault B have

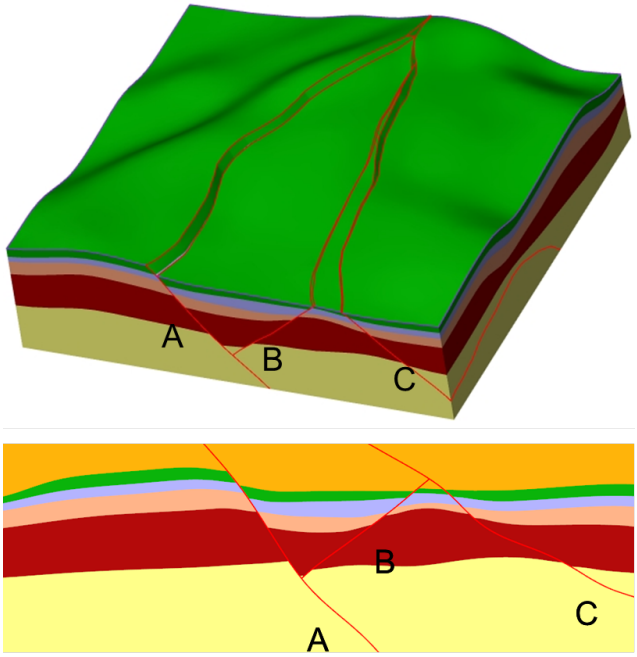

Fig. 19 Displacement for Fault A changed by a factor of 3 with all displacement on hanging wall side. Upper: 3D cube. Lower: Vertical cross section.

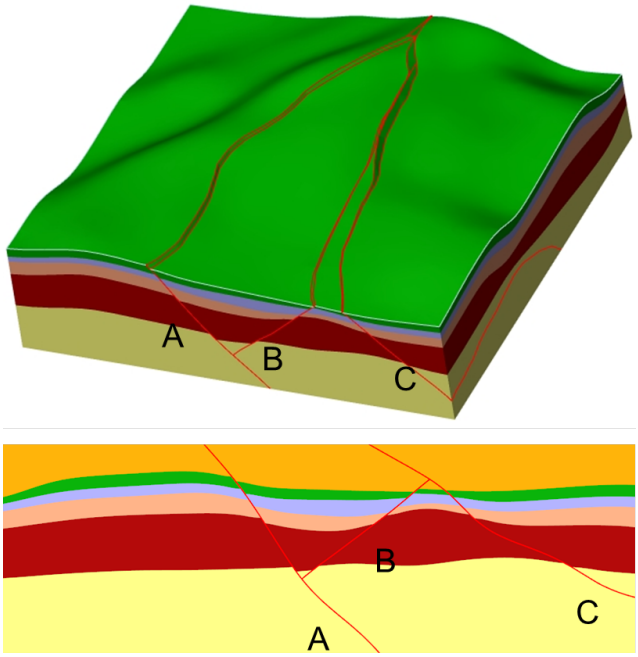

Fig. 20 Displacement for both Fault A and Fault B changed by a factor of 3 with displacement equally distributed on hanging wall and foot wall sides for both fault A and all displacement on hanging wall side for Fault B and equal reverse drag radius. Upper: 3D cube. Lower: Vertical cross section.

changed displacement, but with all displacement on the hanging wall side for Fault B.

The effect of how truncations impact the displacement fields is shown in Figure 22. The original horizons are shown by lines while the colouring of the zones shows the changed positions. In the upper cross section plot, the displacement for Fault B has been increased by a factor of 3 and the displacement is equally distributed on hanging wall and foot wall side of the fault. Even if the distances between Fault B and the other two truncating faults are shorter than the reverse drag radius, the effect of changing the displacement stops at both Fault A and Fault C because of the truncation. This is visible for all horizons. In the lower cross section plot, the displacement for Fault A has been increased by a factor of 3 with all displacement on the hanging wall side and with a long reverse drag ratio. Since Fault B does not truncate A, the change of displacement continues over Fault B, but stops at Fault C which is the truncating fault.

7 Conclusions

A surface based fault method is presented. This model is parametrized in such a manner that the fault can easily change position, orientation and throw by explicitly changing parameter values. This flexibility is an important tool in sensitivity analysis and history matching. The displacement of the volume around the fault is defined as a 3D vector field based on information from intersections between horizons and faults and a parametric formulation of the displacement away from the fault surface. All points affected by the fault can be modified by operations performed on this vector field. The algorithm developed on the basis of the fault model allows points on horizons to be moved according to user-specified changes to the displacement caused by the fault. When several faults are influencing each other, the interactions between them are taken care of by explicit truncation rules, and these rules also influence the displacement fields applied to the horizons. The methodology is demonstrated on synthetic examples based on a fault pattern from a real reservoir.

Acknowledgements The authors want to thank Statoil ASA for financing the project and several persons at Statoil Research Centre in Trondheim for valuable discussions and for providing data and other input to the examples used both in developing and testing of the methodology and for this paper. We will also thank Roxar ASA for good cooperation and support regarding the fault format and structural model in RMS. Finally, The Norwegian Research Council (NFR) is thanked for financing the writing of this article.

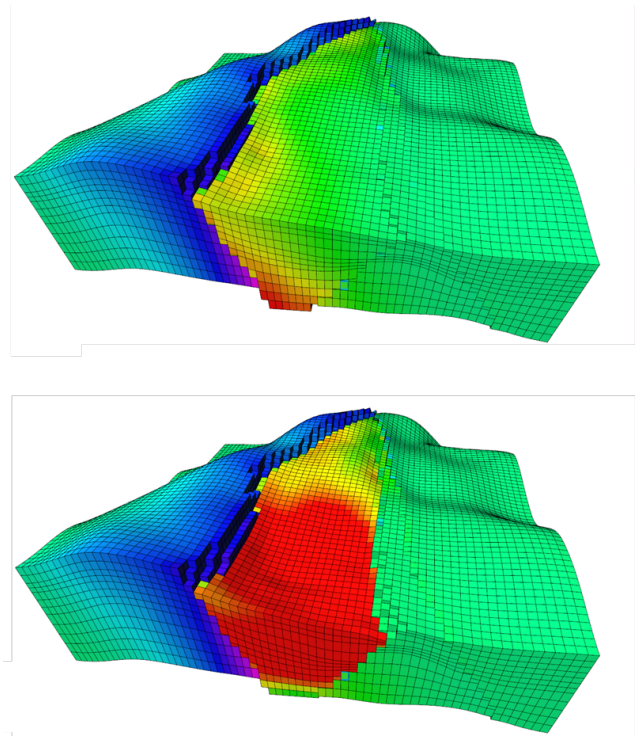

Fig. 21 Gridded reservoir showing cells that are influenced by the change of displacement. Warm colours mean downward displacement. Cold colours mean upward displacement. Upper: Fault A has changed displacement. Lower: Both fault A and fault B has changed displacement

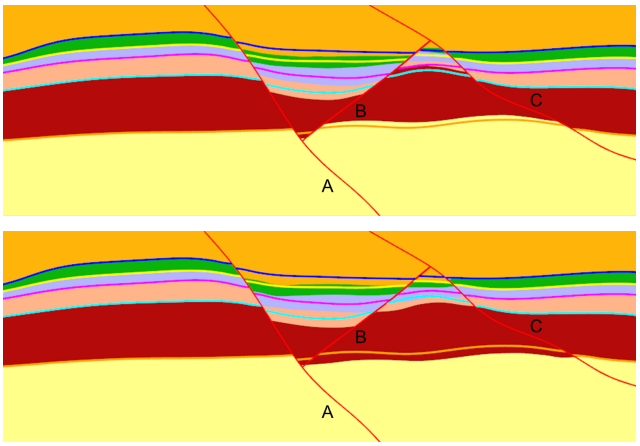

Fig. 22 Effect of truncations on displacement fields. Original horizons shown by lines, modified horizons shown by zone colouring. Upper: The displacement for Fault B is changed by a factor of 3 with equal distribution on hanging wall and foot wall sides. The change of displacement stops at the truncating faults on both sides of Fault B. Lower: The displacement of Fault A is changed by a factor of 3 with all distribution on the hanging wall side and long reverse drag radius. Displacement change continues past Fault B, but stops at Fault C.

References

1. Barnett, J.A.M., Mortimer, J., Rippon, J.H., Walsh, J.J. and Watterson, J.: Displacement Geometry in the Volume Containing a Single Normal Fault. *The American Association of Petroleum Geologists Bulletin*, **71**(8), 925–937 (1987)
2. Cardozo, N., Røe, P., Soleng, H.H., Fredman, N., Tveranger, J. and Schueller, S.: A methodology for efficiently populating faulted corner point grids with strain. *Petroleum Geoscience*, **14**(2), 205–216 (2008)
3. Caumon, G., Lepage, F., Sword, C.H. and Mallet, J.-L.: Building and Editing a Sealed Geological Model. *Mathematical Geology*, **36**(4), 405–424 (2004)
4. Caumon, G., Tertois, A.L., and Zhang, L.: Elements for Stochastic Structural Perturbation of Stratigraphic Models. *EAGE Petroleum Geostatistics*, Extended Abstracts, A02 (2007)
5. Caumon, G., Collon-Dronaillet, P., Le Carlier de Veslud C., Viseur, S. and Sausse J.: Surface-Based 3D Modeling of Geological Structures. *Mathematical Geosciences*, **41**(8), 927–945 (2009)
6. Gibson, J.R., Walsh, J.J. and Watterson, J.: Modelling of bed contours and cross-sections adjacent to planar normal faults. *Journal of Structural Geology*, **11**(3), 317–328 (1989)
7. Goovaerts, P.: Geostatistics for Natural Resources Evaluation. *Oxford University Press*, 125–184 (1997)
8. Hoffman, K.S. and Neave, J.W.: The fused fault block approach to fault network modelling. In: Jolley, S.J., Barr. D., Walsh, J.J. and Knipe, R.J. (Eds) *Structurally Complex Reservoirs.* Geological Society, London, Special Publication **292**, 75–87 (2007)
9. Holden, L., Mostad, P., Nielsen, B.F., Gjerde, J., Townsend, C. and Ottesen, S.: Stochastic Structural Modeling. *Mathematical Geology*, **35**(8), 899–914 (2003)
10. Hollund, K., Mostad, P., Nielsen, B.F., Holden, L., Gjerde, J., Contursi, M.G., McCann, A.J., Townsend, C. and Sverdrup, E.: Havana - a fault modeling tool. In: Koestler, A.G. and Hunsdale, R. (Eds.) *Hydrocarbon Seal Quantification.* Norwegian Petroleum Society (NPF), Special Publications, **11**, 157–171 (2002)
11. Lecour, M., Cognot, R., Duvinage, I., Thore, P. and Dulac, J-C.: Modeling of stochastic faults and fault networks in a structural uncertainty study. *Petroleum Geoscience*, **7**, S31–S42 (2001)
12. Mallet, J.-L.: Space-time mathematical framework for sedimentary geology. *Mathematical Geology*, **36**(1), 1–32 (2004)
13. Manzocchi, T., Heath, A.E., Palananthakumar, B., Childs, C. and Walsh, J.J.: Faults in conventional flow simulation models: a consideration of representational assumptions and geological uncertainties. *Petroleum Geoscience*, **14**(1), 91–110 (2008)
14. Rivenæs, J.C., Otterlei, C. Zachariassen, E., Dart, C. and Sjøholm, J.: A 3D stochastic model integrating depth, fault and property uncertainty for planning robust wells, Njord Field, Offshore Norway. *Petroleum Geoscience*, **11**(1), 57–65 (2005)
15. RMS 2010.1 User guide. *Roxar Software Solutions, Stavanger, Norway* (2010)
16. Røe, P., Abrahamsen, P., Georgsen, F., Syversveen, A.R. and Lia, O: Flexible Simulation of Faults. *SPE Annual Technical Conference and Exhibition, Florence, Italy, 19-22 September*, SPE 134912 (2010)
17. Seiler, A., Rivenæs, J.C., Aanonsen, S.I. and Evensen, G.: Structural Uncertainty Modelling and Updating by Production Data Integration. *SPE/EAGE Reservoir Characterization and Simulation Conference, Abu Dhabi, UAE, 19-21 October*, SPE 125352 (2009)

18. Seiler, A., Aanonsen, S.I., Evensen, G. and Lia, O.: An elastic grid approach for fault uncertainty modelling and updating using the Ensemble Kalman filter *SPE Europec/EAGE Annual Conference and Exhibition, Barcelona, Spain, 14-17 June*, SPE 130422-PP (2010)
19. Thore, P., Shtuka, A., Lecour, M., Ait-Ettajer, T. and Cognot, R.: Structural uncertainties: Determination, management, and applications. *Geophysics*, **67**(3), 840–852 (2002)
20. Yielding, G., Freeman, B. and Needham D.T.: Quantitative Fault Seal Prediction. *The American Association of Petroleum Geologists Bulletin*, **81**(6), 897–917 (1997)
21. Walsh, J.J. and Watterson, J.: Distributions of cumulative displacement and seismic slip on a single normal fault surface. *Journal of Structural Geology*, **9**(8), 1039–1046 (1987)
22. Walsh, J.J. and Watterson, J.: Displacement gradients on fault surfaces. *Journal of Structural Geology*, **11**(3), 307–316 (1989)